Journal of Energy Storage 102 (2024) 114149

Contents lists available at ScienceDirect

Journal of Energy Storage

journal homepage: www.elsevier.com/locate/est

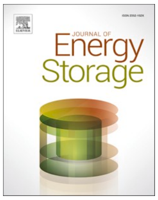

Research papers

Self-charging integrated energy modules: A record photoelectric storage efficiency of 14.6 %

Jae-Kwang Kim [a,1], Jun Ryu [b,1], Chaeeun Kang [a], Jooeun Park [a], Jeha Kim [a], Jung Sang Cho [c], Dong-Won Kang [b,d,*], Sang Mun Jeong [e,**]

[a] Department of Energy Convergence Engineering, Cheongju University, Cheongju, Chungbuk 28503, Republic of Korea
[b] Department of Smart Cities, Chung-Ang University, Seoul, Republic of Korea
[c] Department of Engineering Chemistry, Chungbuk National University, Chungbuk 28644, Republic of Korea
[d] Department of Energy Systems Engineering, Chung-Ang University, Seoul, Republic of Korea
[e] Department of Chemical Engineering, Chungbuk National University, Chungdae-to 1, Seowon-Gu, Cheongju, Chungbuk 28644, Republic of Korea

ARTICLE INFO

Keywords:
Integrated energy modules
Perovskite
lithium sulfur
Self-charging
Metal patterning
Photoelectric storage efficiency

ABSTRACT

As portable electronic devices typically rely on rechargeable batteries, it inherently limits their operational time. A promising approach to overcome this limitation is the integration of energy conversion and storage devices, thereby enabling semi-permanent usage of portable electronics. A novel integrated energy module is presented, which demonstrates a high photoelectric storage efficiency (PSE). This module comprises a perovskite solar cell (PSC) as the energy converter and a lithium-sulfur battery (LSB) as the storage unit. In our configuration, four series-connected PSCs provide a high open-circuit voltage (V_{OC}) of 4.5 V and a conversion efficiency of 16.2 % with a 1 cm^2 area. The PSC-LSB module achieves an unprecedented PSE of 14.6 % among LSB-based integrated energy modules, marked by a significant output voltage of 2.1 V at a current density of 0.16 A/g. Additionally, we report an 87 % retention capacity for the PSC-LSB module, which utilizes a lithium metal anode and sulfur-composited porous carbon fibers cathode. This module maintains stable performance over 200 cycles. The superior characteristics of the PSC-LSB energy integrated module can be attributed to the efficient engineering of each PSC and LSB device, as well as effective metal patterning connections on the common electrode/substrate.

1. Introduction

Energy is indispensable for human life and plays a pivotal role in modern industry. High-tech industries such as the Internet of Things (IoTs), artificial intelligence (AI), unmanned aerial vehicles (UAVs), and robots are major components of the Fourth Industrial Revolution, profoundly influencing our daily lives. However, these advancements pose new challenges for energy technology. Wireless communication devices that transmit substantial data over a broad area require a continuous and portable power supply. [1–3] Although electricity is commonly provided through long-distance cables, spatial constraints exist. While energy storage devices can address these limitations, portable electrochemical storage devices necessitate frequent recharging or replacement. While portable energy storage devices have fueled the portable information era, they are insufficient for meeting the demands of future electronic devices. [4] Time constraints also arise during usage after charging. Large-sized energy storage devices are employed as distributed power sources alongside renewable energy sources. Nevertheless, distributed renewable energy, such as wind and solar power, is inherently unstable, subject to variations based on the time of day, weather conditions, and location. [5,6] Consequently, the integration of energy harvesting and storage devices has become imperative to ensure a stable power supply to portable electronic devices. This integration refers to a power device that combines energy harvesting and storage for self-charging purposes. [7–9] Such integrated energy devices can accumulate and store electricity produced by the energy harvester, providing a stable power supply for a defined period. Power management circuitry, handling AC-DC conversion, DC-DC conversion, power matching, impedance matching, etc., is typically essential in these integrated energy devices. Solar cells serve as energy harvesters, and

---

* Correspondence to: D.-W. Kang, Department of Energy Systems Engineering, Chung-Ang University, Seoul, Republic of Korea.
** Corresponding author.
E-mail addresses: kangdwn@cau.ac.kr (D.-W. Kang), smjeong@chungbuk.ac.kr (S.M. Jeong).
[1] The first and second authors have equal contribution.

https://doi.org/10.1016/j.est.2024.114149
Received 9 April 2024; Received in revised form 24 July 2024; Accepted 9 October 2024

lithium (Li) secondary batteries or capacitors serve as energy stores in integrated energy modules for self-charging. Within these integrated energy modules, the photoelectric storage efficiency (PSE) is a crucial property for continuous power supply to electronic devices. However, reported integrated energy modules have shown PSE lower than 10 % and low energy density. [5,7–13] In the pursuit of enhancing both photoelectric conversion efficiency (PCE) and energy density within integrated energy modules, it is imperative to prioritize the utilization of high-efficiency solar cells and high-capacity rechargeable batteries. One compelling solar cell that stands out for on-chip integrated energy modules involves integrating perovskite solar cell (PSC) as energy harvesters. Recently, PSCs have exhibited a high PCE of about 26.1 %, attributed to their exceptional optoelectronic properties. [14–21] In addition, their unique characteristics, including tunable bandgaps, [17] high open circuit voltage (V_{OC}), [22] lightweight nature, [23] and cost-effectiveness in fabrication, [24] render them exceptionally well-suited for integration with energy storage devices, such as batteries. This strategic amalgamation of lithium sulfur (S) battery (LSB) and PSC development forms a symbiotic relationship between solar cells and batteries, suggesting a promising way to address the problems associated with variability in solar energy.

In this study, we achieved a self-charging feature through the integration of a bifunctional energy harvesting and storage power source based on a PSC-driven photo-rechargeable lithium-sulfur battery system (PSC-LSB). For the photovoltaic (PV) unit, we developed an ultrathin PSC with a PCE approaching 18 %. Moreover, four interconnected PSCs provided a high V_{OC} of 4.5 V at an active area efficiency of 16.2 %. In the energy storage unit, we introduce the first use of a lithium-sulfur battery, demonstrating high-capacity, high-energy characteristics, and stable performance under mechanical deformation. Consequently, the PSC-LSB integrated system achieved an unprecedented PSE of 14.6 %, surpassing any energy integrated modules employing LSB reported to date. A high output voltage of 3 V at a discharge current density of 0.1C was also observed. Remarkably, it maintained an overall efficiency exceeding 10 %, even at the high current density of 1C, outperforming state-of-the-art photo-charging power sources reported to date. Our results suggest that PSC-LSB devices represent an innovative class of integrated energy harvesting and storage systems with safety and durability advantages, offering significant benefits toward practical self-powered electronics.

2. Experimental section

2.1. Materials

We used commercial materials without any further treatment. Formamidinium iodide (FAI, 99 %, Greatcell Solar Materials), cesium bromide (CsBr; 99.999 %, Alfa Aesar), lead iodide (PbI_2; 99.99 %, Tokyo Chemical Industry), lead bromide ($PbBr_2$; 99.999 %, Sigma-Aldrich), and n-butylammonium iodide (BAI; 99 %, Greatcell Solar Materials) were used for the perovskite absorber layer. Dimethylformamide (DMF; 99.5 %, Samchun Chemicals) and dimethyl sulfoxide (DMSO; 99.8 %, Samchun Chemicals) were used as perovskite precursor solvents. Nickel (II) nitrate hexahydrate ($Ni(NO_3)_2$ $6H_2O$; 99.999 %, Sigma-Aldrich), ethylene glycol (EG; 99.8 %, Samchun Chemicals), and ethylenediamine (EDA; 99 %, Samchun Chemicals) were used for the hole transport layer. The 2-(3,6-Dimethoxy-9H-carbazol-9-yl)ethyl)phosphonic acid (MeO-2PACz; 98 %), Phenyl-C_{61}-butyric acid methyl ester ($PC_{61}BM$; 99.5 %) and bathocuproine (BCP; 99 %) were purchased from OSM, a Korean company, for the self-assembled monolayer (SAM), electron transport layer and buffer layer, respectively. Ethanol (EtOH; 99.9 %, Sigma-Aldrich), chlorobenzene (CB; 99.8 %, Wako Chemical Industries) and 2-propanol (IPA; 99.5 %, Sigma-Aldrich) were used as solvents respectively. Indium doped tin oxide (10 Ω/sq) coated glass substrates were purchased from AMG, a Korean company. Polyvinyl alcohol (PVA; PVA 2000, Kanto chemical Co., INC.), EtOH (≥99.9 %, Duksan), polystyrene (PS; Yakuri Pure Chemicals Co., Ltd.), sulfur (S, 99.5 %, Sigma-Aldrich), and *N*-methylpyrrolidone (NMP, 99.5 %, Samchun Pure Chem. Co., Ltd.) were purchased for the LSB fabrication.

2.2. Device fabrication for PSC

2.2.1. Precursor solution synthesis

The NiO_x precursor solution was prepared by dissolving 0.8 mmol Ni $(NO_3)_2$ in a mixture of 1 mL of EG and 53.6 μL of EDA. The perovskite precursor solution generated with two step process. First, FAI (0.83 M), CsBr (0.17 M), PbI_2 (0.83 M), and $PbBr_2$ (0.17 M) were dissolved in DMF/DMSO mixture solvent (ratio is 4:1) for FACs-based precursor solution. Next, BA-based precursor solution was manufactured BAI (1.00 M), PbI_2 (0.75 M), and $PbBr_2$ (0.25 M) by in the same solvent of FACs-based precursor solution. Finally, mix the FACs-based and BA-based precursor solutions in a ratio of 98:2, a perovskite precursor solution with a composition of $BA_{0.02(}FA_{0.83}Cs_{0.17})_{0.98}Pb(I_{0.83}Br_{0.17})_3$ was prepared.

2.2.2. PSC fabrication methods

The ITO glass substrates were cleaned by ultrasonication in acetone and IPA, respectively, for 15 min each. After drying, the substrates were treated with ultraviolet-Ozone UV-O_3 for 25 min. The NiO_x precursor solution was spin-coated onto the UV-O_3-treated substrate at 5000 rpm for 50 s and annealed on a hotplate set at 300 °C for 60 min. After the NiO_x-coated substrates were cooled down to room temperature, MeO-2PACz solution (0.4 mg/mL in EtOH) was spin coated onto the NiO_x-coated substrate at 5000 RPM for 20 s and annealed at 150 °C for 5 min. After the process is over, substrates were transferred into a nitrogen-filled glove box for the next process. The perovskite precursor solution was spin-coated onto the substrate at 4000 RPM for 30 s, with 0.3 mL of anisole being dripped onto the substrate at 25 s from the start of spinning, and then annealed at 75 °C and 110 °C for each 1 min and 10 min respectively. Subsequently, the $PC_{61}BM$ (20 mg/mL dissolved in CB) was spin-coated on the perovskite film at 1500 RPM for 30 s and annealed at 110 °C for 10 min. Then, BCP solution (0.5 mg/mL dissolved in IPA) was spin coated onto the $PC_{61}BM$ coated substrate at 4000RPM 30 s and annealed at 110 °C for 5 min. Finally, Cu electrodes were deposited using a thermal evaporator with a shadow mask.

2.2.3. LSB fabrication methods

Porous carbon fiber was prepared through electrospinning process. The precursor electrospinning solution was prepared by dissolving PVA into EtOH solution, and then PS nanobeads added into the resulting solution with vigorous stir overnight. The obtained aqueous suspension was loaded into a syringe matched with needle. A high voltage of 18 kV was applied. The synthetic PVA/PS fibers were stabilized in a furnace at 100 °C for 24 h in air, and then carbonized at 600 °C for 5 h at a heating rate of 5 °C/min under N_2 atmosphere. Sulfur was encapsulated in the porous carbon fiber film using solution-diffusion method using carbon disulfide solvent. The as-prepared S-CC66 was mixed with porous carbon fiber (CC66) and sulfur in a weight ratio of 1:4. The mixture was heated at 160 °C for 12 h under nitrogen atmosphere.

The prepared sulfur electrode was composed of the S-CC66, poly (vinylidene fluoride) (PVDF), and Super-P carbon black (weight ratio of 70:10:20). Three composite materials were mixed in NMP, followed by coating on an Al current collector and drying at 60 °C for 12 h in vacuum. The Sulfur cathode was active material loading of 6 mg/cm^2 and assembled with lithium metal anode (1 mm) and hybrid solid electrolyte based Lithium Aluminum Titanium Phosphate (LATP), PVDF and 1 M lithium bis(trifluoromethylsulfonyl)imide (LiTFSI) salt in a mixed solvent of tetraethylene glycol dimethyl ether (TEGDME) and 1,3-dioxolane (DOL) (1/1, v/v) electrolyte (70:10:20 wt%). [25]

2.3. *Characterization*

All measurements were executed in ambient air except for those requiring measurements under vacuum. J-V curve of the PSC single cell and module were measured using a light-emitting diode (LED) solar simulator (LSH-7320, Newport Corporation) under standard AM 1.5 illumination (100 mW/cm^2) The external quantum efficiency (EQE) spectrum was characterized using a monochromator (DongWoo Optron, MonoRa500i) and light source (Abet Technologies 150 W xenon lamp, 13014) with a CompactStat instrument (Ivium Technologies). The electrode surface morphologies were investigated by field emission scanning electron microscope (FE-SEM; JSM-6700F, JEOL, Japan), and the internal structural characteristics were recorded by transmission electron microscopy (TEM; JEM 3010, JEOL, Japan). The sulfur content in the S-CC66 composite was measured by thermogravimetric (TG) analysis (SDT Q600, TA Instruments, USA). The crystal structures and impurity were characterized using X-ray diffraction (XRD; D/Max 2500/PC, Rigaku, Japan).

3. Result and discussions

The combination of an energy harvesting device and an energy storage cell results in the realization of an integrated energy module design. This module has the potential to function as a sufficient energy source with internal storage for surplus energy. Integrated PV-rechargeable battery (PV-RB) systems offer a compact and energy-efficient alternative to conventional PV-RB counterparts. Fig. 1 depicts a schematic diagram of the rechargeable LSB and PSC integrated energy device, along with the overall circuit diagram. A common patented substrate, consisting of copper coating on polyimide (PI) polymer film, was prepared to serve as the shared foundation between the PSC and LSB (Fig. 1(a)). This copper-patterned PI common substrate functions as the electron current collector for the PSC and the anode current collector for the LSB.

In this work, a DC-DC converter and controller circuit were designed to operate by optimizing the self-operating properties of the energy harvest and energy storage systems, eliminating the need for an additional controller. Electrons and holes generated in the PSC are separated and flow into the anode and cathode of the LSB, respectively. The generated electrons in the PSC transfer to the anode without wiring, facilitating the self-charging process in the LSB. Li_2S is oxidized at the cathode, with lithium-ion extraction during the charging process. Subsequently, the lithium metal anode is reduced at the anode through the lithium-ion insertion process. The self-charging integrated energy device of PSC-LSB is sealed with a polyethylene terephthalate (PET) protective polymer layer through a lamination process on both the PSC and LSB sides. The integrated PSC-LSB systems can be classified into three electrode configurations. In the three-electrode configuration, the central electrode is shared between the two energy systems, serving as the anode for both the PSC and LSB devices. Fig. 1(b) illustrates the overall circuit diagram with a LED load. The black box line represents the equivalent circuit parts, comprising the PSC and LSB in the integrated self-charging energy device shown in Fig. 1(a). Additionally, a rectifying diode is connected between the PSC and LSB to prevent undesirable current flow from the LSB to the PSC, providing protection in dark conditions. In conditions where there is no light to generate electricity, such as in darkness, the PSC does not produce power. In such situations, the LED can be illuminated by turning on a switch, and this is achieved through the discharging mode of the LSB. When sufficient light is insolated, the photo-voltage of the PSC increases beyond the extent of LSB voltage and diode turn-on voltage. Subsequently, the PSC enters solar charging mode, initiating the collection of harvested electrons and holes. These are collected in the patterned copper common substrate and transferred to the lithium metal anode and Li_2S cathode, respectively. The integration of these processes enables the self-charging integrated energy device to efficiently manage energy flow between the PSC and LSB for continuous and reliable operation.

Due to the potential for lithium-ion deintercalation in LSBs within the range of 2.2 V to 2.4 V, it is imperative to have a higher output voltage from the PSC. To ensure stable charging of the LSB, a target voltage for maximum power (V_{mp}) from the PSC was set to a value exceeding 3.0 V. This requirement drove the development of a series connection of 4-unit cells to facilitate efficient charging of the LSB by the PSC. The designed unit cells measure 0.5 cm × 0.5 cm (0.25 cm^2) in size and are connected in series, resulting in a total active area of 1 cm^2. In addition to the necessary output voltage from the PSC, stable carrier generation in the PSC is crucial to support our PSC-LSB energy integrated module. Therefore, in the ABX_3 metal halide perovskite network, an optimized ratio of n-Butylammonium (BA), formamidinium (FA), cesium (Cs), lead (Pb), iodine (I), and bromine (Br) was employed. This optimized ratio was used to construct a $BA_{0.02}(FA_{0.83}Cs_{0.17})_{0.98}Pb(I_{0.83}Br_{0.17})_3$ 3D perovskite architecture, achieving a suitable bandgap energy of 1.63 eV. This specific configuration aims to strike a balance between V_{OC} and PCE of the PV cell. Furthermore, a SAM of MeO-2PACz was employed between the NiO_x hole transport layer and the perovskite to enhance hole extraction properties [26]. For efficient electron collection, a conventional $PC_{61}BM$/BCP bilayer was utilized to ensure efficient electron transfer and suitable hole blocking, [27] as illustrated in the device structure shown in Fig. 2(a). The 1-sun PV performance of the unit PSC was characterized by a J-V curve with forward and reverse scans, as depicted in Fig. 2(b). The unit PSC, with a size of 0.04 cm^2, exhibited a PCE of 18.19 %, short-circuit current density (J_{SC}) of 20.49

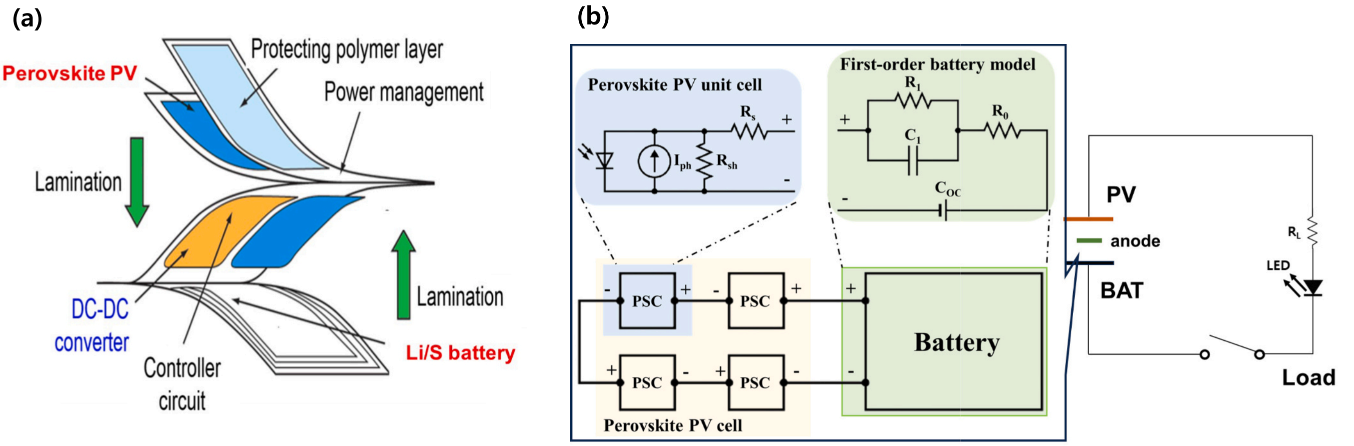

Fig. 1. (a) Schematic diagram of energy integrated modules consisting of perovskite photovoltaics (PV) and lithium (Li)/sulfur(S) battery, and (b) equivalent circuit diagram of the energy integrated modules.

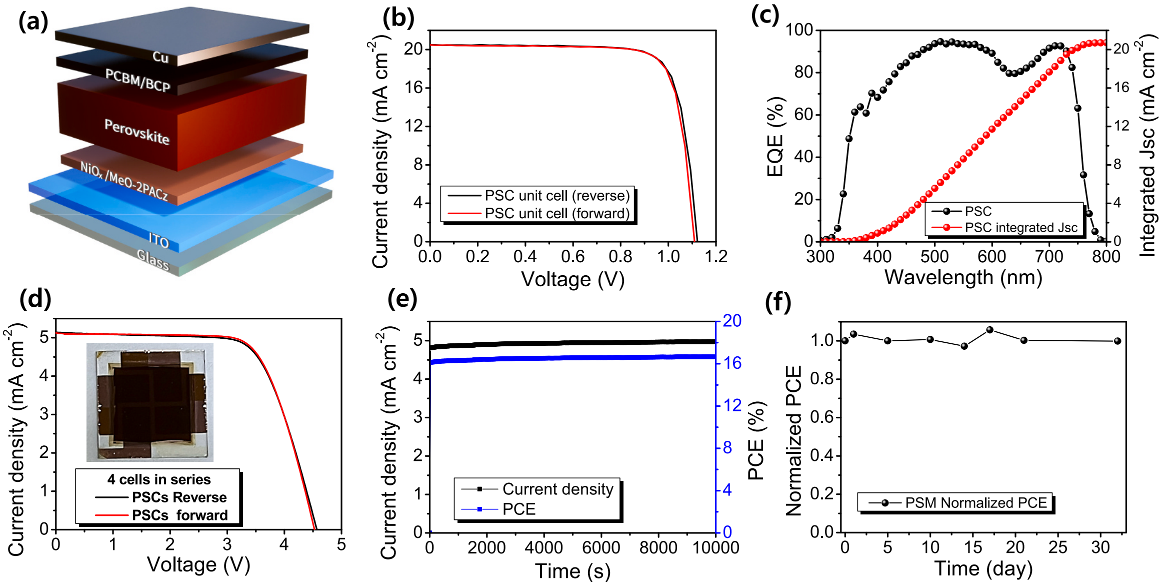

Fig. 2. (a) Illustrated in the photovoltaic device structure (b) current density-voltage curves, (c) external quantum efficiency and integrated J_{SC} of PSC unit cell. (d) current density-voltage curves, (e) steady-state photocurrent and power output, (f) long-term stability of series-connected arrangement of four PSCs.

mA/cm^2, open-circuit voltage (V_{OC}) of 1.11 V, and fill factor (FF) of 80.00 %, respectively. Regarding EQE, strong visible light absorption was observed with a negligible integrated J_{SC} value compared to the one extracted from the J-V measurement using a solar simulator. To deliver a suitable voltage to the LSB, the performance of a series-connected arrangement of four PSCs was also monitored (refer to the inset image in Fig. 2(d)). The results revealed a commendable PV performance with an V_{OC} of 4.53 V, J_{SC} of 5.13 mA/cm^2, FF of 69.97 %, and PCE of 16.24 %, based on an active area of 1 cm^2. It's worth noting that the series-connected PSCs exhibited a decrease in FF compared to the unit PSC, which is expected to be further reduced by suppressing the series resistance caused by an elongated indium tin oxide (ITO) path [28]. Despite this, both the unit PSC and series-connected PSCs show only minor hysteresis, allowing for accurate analysis of the PSC-LSB system.

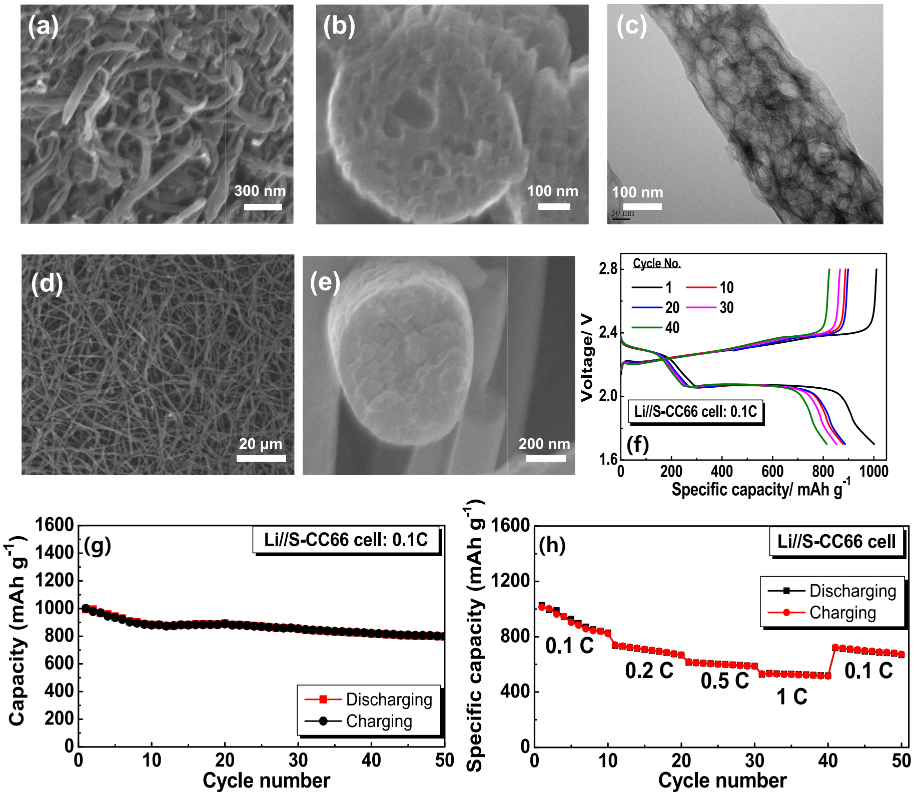

Fig. 3. Field Emission Scanning Electron Microscope (FE-SEM) image of (a) porous carbon fiber (CC66) and (b) magnified view of cross section and surface. (c) Transmission electron microscopy (TEM) of CC66. FE-SEM image of (d) sulfur-composited CC66 and (e) magnified view of cross section and surface. (f) Charge-discharge voltage profiles and (g) Cycling performance of the Li/S-CC66 cell at 0.1C. (h) Rate performance of the Li/S-CC66 cell at 0.1–1C-rate.

Operational stability was further assessed to evaluate the capability of the PSC for stable deintercalation in the battery. In Fig. 2(e), the steady-state photocurrent and power output of the fabricated PSC without encapsulation were measured near the maximum power output voltage of 3.35 V under AM 1.5 illumination for 10,000 s. The results indicate highly stable photocurrent and power output under ambient air conditions with a relative humidity (R.H.) of approximately 30 %. This suggests promising operational stability for the PSC in the PSC-LSB integrated system. Additionally, Fig. 2(f) illustrates the long-term stability of the PSC collected under a nitrogen (N_2) filled glove box. The PSC demonstrated exceptional reliability of output performance for 32 days without degradation. Therefore, the designed $BA_{0.02}(FA_{0.83}Cs_{0.17})_{0.98}Pb(I_{0.83}Br_{0.17})_3$-based inverted planar type PSCs exhibit satisfactory operation, making them applicable for integrated energy modules. This extended stability under controlled conditions enhances the feasibility of the PSC for long-term use in practical applications within integrated energy systems.

To prepare high-performance LSBs, sulfur was introduced into porous carbon fiber (CC66) through a process involving electrospinning and the sulfur solution-diffusion method. [29] Fig. 3(a) displays a FE-SEM image of the prepared porous carbon fiber, revealing a fibrous morphology with an approximate diameter of 320 nm. In Fig. 3(b), a magnified view of the cross-section and surface of the porous carbon fiber is provided, showcasing numerous pores embedded within the carbon fibers and a multitude of nanopores distributed across the surface. The carbon fiber constructs a three-dimensionally interlacing network structure, promoting accelerated electron/ion transfer, while the pores offer sufficient space to accommodate the active material and adsorb polysulfides, thereby enhancing the reutilization of the active material. The internal structure of the porous carbon fiber was further examined using TEM, as shown in Fig. 3(c). The TEM image reveals a visually striking 3D networked nanoporous structure within the carbon fibers, aligning with the cross-sectional view of CC66 displayed in Fig. 3 (b). Sulfur-composited porous carbon fiber was synthesized through a solution-diffusion method. Elemental sulfur was mixed with porous carbon fiber and then imbibed into the pores in CC66 by capillary forces above the melting point (155 °C). This approach facilitates the incorporation of sulfur into the porous carbon structure, contributing to the overall performance and efficiency of the resulting lithium-sulfur batteries. As depicted in Fig. 3(d), the sulfur-composited porous carbon fiber maintains its fibrous morphology without any visible aggregation of sulfur particles on the surface of the porous carbon fiber. This observation indicates that sulfur has been effectively encapsulated within the carbon matrix. Further magnified images of the cross-section and surface of sulfur-composited porous carbon fiber are presented in Fig. 3(e). These images reveal a smooth surface without any particle aggregations, suggesting that sulfur infiltration occurred within the carbon matrix rather than on its surface. The presence of sulfur atoms in the porous carbon is confirmed using SEM–EDS mapping of the sulfur-composited CC66 (S-CC66) (Fig. S1). In Fig. S1(b-c), the red and green regions denote carbon and sulfur, respectively. Therefore, sulfur atoms are uniformly dispersed in the porous carbon fiber. To confirm the porous properties of the CC66, N_2 adsorption–desorption isotherms and pore size distributions were studied, as shown in Fig. S2. The CC66 exhibited 245 $m^2\ g^{-1}$ surface area, high pore area (117.5$m^2\ g^{-1}$) and 23.8 nm average pore size. The sulfur content by weight percent is consistent with the TG result (Fig. S3(a)). Compared to the synthesis method provided for S-CC66 in the experimental section, the loss of sulfur may be due to its property of evaporating even at lower temperatures. The S-CC66 comprised 66 wt% by weight difference before and after the sulfur composite reaction. The formation of the porous carbon, sulfur powder, and S-CC66 composite is confirmed using XRD in Fig. S3 (b). The diffraction peaks of S-CC66 correspond well with the sulfur patterns (JCPDS card no. 08–0247), indicating that sulfur impregnated on the porous carbon fiber is mainly in the form of S8. The charge–discharge voltage profiles of the Li/S-CC66 cell at 0.1C are depicted in Fig. 3(f). The curves exhibit two reduction plateaus at 2.29 V and 2.07 V, respectively, corresponding to the formation of long-chain polysulfides (Li_2S_x, $4 \leq x \leq 8$) and the conversion of Li_2S_x to Li_2S_2/Li_2S. These reduction plateaus are consistent with the typical double-platform discharge behaviors observed in charge-discharge curves. The complete upper discharge plateaus suggest that migrating polysulfides are localized in the cathode region, and severe active material loss has not occurred. The appearance of the vertical voltage rise at 2.8 V indicates a complete charge process. The initial discharge capacity of the cell with CC66 reservoirs is 1001.1 mAh/g, which approaches 60 % of the theoretical capacity of sulfur (1675 mAh/g). The high active material utilization is a result of improved cathode conductivity achieved by encapsulating the active material in the conductive CC66 reservoir. The cycling performance in Fig. 3(g) reveals that the cells with CC66 reservoirs exhibit high discharge capacity, stable cyclability, and high Columbic efficiency of >99 % for over 50 cycles. After 50 cycles, the discharge capacity of the cells approaches 791 mAh/g with a capacity degradation rate of 0.41 % per cycle. Fig. 3(h) indicates the rate performance of the Li/S-CC66 batteries at current densities of 0.1–1C-rate. Reversibility is the ratio of discharge capacity to charge capacity and is higher than 99 % in all C-rate. The reversible discharge capacities of the Li/S-CC66 battery are 1007.1, 735.3, 614.4, and 528.4 mAh/g at constant current rates of 0.1, 0.2, 0.5, and 1C, respectively, with a rate capability retention of 88 % (10th/41st cycles at 0.1C). The stable cyclability and high-capacity retention result from the synergistic effects of the natural mesopores and the long-range porous network of CC66. The natural pores in the carbon fiber are critical for accommodating the active material and absorbing polysulfides during cycling, as extensively examined in the literature. [30–32] Therefore, the CC66 current collectors store active material, and the CC66 inhibitors intercept migrating polysulfides, suppressing the loss of active material and offering excellent cycle stability. The intimate contact between the electrolyte and sulfur-impregnated carbon fiber facilitates electron transfer in the inactive area, as evidenced by the unchanged low resistances of CC66 reservoirs. EIS measurement demonstrated the high electrochemical kinetics of the S-CC66 cell. The left semicircle in the high-frequency region shows the charge transfer resistance (R_{ct}), whereas the right sloping line in the low-frequency region is related with ion diffusion as Warburg impedance. A larger Warburg slope indicates higher ion diffusion coefficient [33]. As shown in Fig. S4, in the initial state, the R_{ct} of the S-CC66 cell is smaller than those of the bare cell, indicating S-CC66 cell achieves higher conductivity and faster ion diffusion. The redox reactions of the S-CC66 cell were investigated by CV measurement at a scan rate of 0.05 mV S^{-1} (Fig. S5). Two distinct cathodic peaks at 2.0 V and 2.3 V indicate the conversion from elemental sulfur (S_8) to highly ordered soluble polysulfide and subsequently to insoluble polysulfide (Li_2S) during reduction. The S-CC66 cell was operated stably without change up to 10 cycles. For the integrated PSC-LSB energy module, the sulfur cathode was fabricated using a mixture of PVDF, and Super-P carbon black in a weight ratio of 70:10:20. The cathode was cut into a size of 3.5 cm × 3.5 cm with a sulfur loading amount of 6 mg/cm^2 (Fig. S6(a)), designed for a capacity of 74 mAh in a monolayer cell (Fig. S6(b)). The lithium metal anode was designed to a size of 4 cm × 4 cm to prevent side reactions on the edge by staggered lamination of electrodes.

To ensure efficient constant self-charging of the LSB, the current and voltage of both the PSC and LSB must be optimized. The charging curve of the energy storage part (LSB) should overlap with the photocurrent–voltage curve of the energy conversion part (PSC) to identify the efficient operation region, as demonstrated in Fig. 4(a). The green area represents the efficient self-charging region range that can supply a constant current. The power is limited to a maximum of 15 mW/cm^2, and the charge potential of the battery is restricted to 3.0 V. If the charge potential exceeds 3.0 V, the current is irregularly supplied, potentially causing damage to the electrode. To fabricate a stable integrated energy module, the energy storage system needs to be optimized at 3.0 V, and

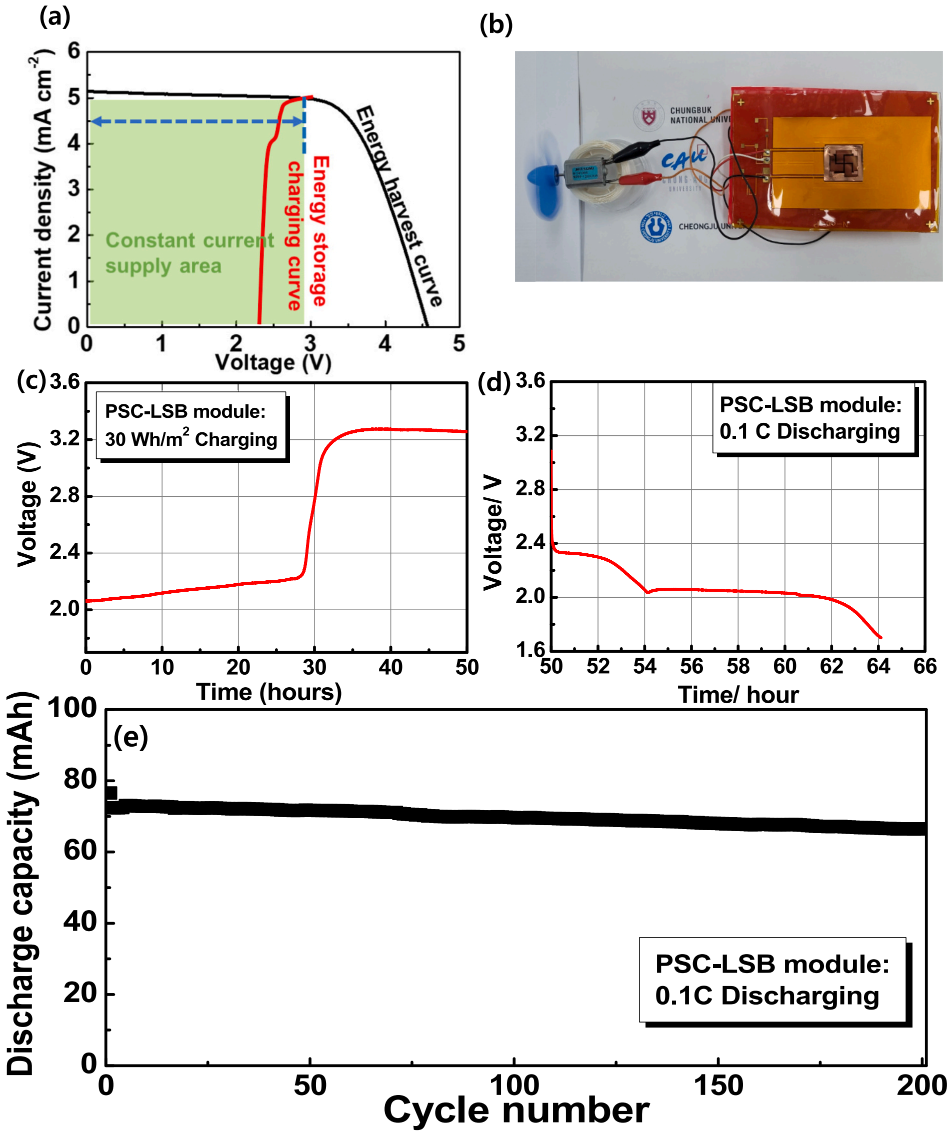

Fig. 4. (a) Overlapping Charging Curve of the LSB with the photocurrent–voltage curve of PSC. (b) Digital photograph of on-chip integrated PSC-LSB energy module. (c) Charging curve of the LSB in the PSC-LSB energy module during light source supply. (d) Discharging curve of the PSC-LSB energy module at 0.1C after self-charging. (e) Cycle stability of the PSC-LSB energy module with discharge capacity at 0.1C.

sufficient current is stored to provide ample electricity. Consequently, a sulfur battery (with a charging potential <3.0 V) was employed for the energy storage part of the integrated energy module. For the on-chip integrated PSC-LSB energy module, copper (Cu) was patterned on the PI substrate. The Cu patterned area in the center of the PI substrate serves as the common substrate, used as the electron collector of the n-type electrode of the PSC and the anode current collector with lithium metal of the LSB. On the front, the PSC is bonded onto the patterned Cu substrate, and the n-type electrode faces downward (Fig. S7(a)). The p-type electrode of the PSC is connected to the cathode of the backside LSB through an on-chip upper-right direction (Fig. S7(b)). The tap of the backside LSB is connected to the upper-right direction (cathode) and the bottom-right direction (anode), where an electric fan is connected to receive electricity. In addition, a demonstration of electric fan operation using the PSC-LSB energy module is shown in the video 1 of Supplementary Information. A crucial consideration in this part is that the patterned Cu should be in good contact with both sides, and there should be no holes through the patterned Cu edges. This is essential to prevent any material movement between the energy harvesting and energy storage parts. Fig. S8 illustrates the process of photo-to-electric conversion for charging the integrated PSC-LSB energy module using the designed PSCs. The integrated PSC-LSB energy module was then encapsulated with a PET film, as shown in Fig. 4(b). Each side of the integrated PSC-LSB energy module was sealed with ethylene vinyl acetate (EVA) through hot-pressing. To investigate the electrochemical properties of the integrated PSC-LSB energy module, a 30 Wh/m^2 light source was supplied to the front PSC side, and the LSB was charged with a self-current storage through a patterned Cu current collector on an on-chip common substrate. Fig. 4(c) presents the charging curve of the energy storage part (LSB) in the PSC-LSB energy module during the supply of a light source. The analysis was conducted to observe changes in voltage over time, and the LSB was fully charged in 30 h. The supplied current from PSC is almost same with 0.03C of LSB. The charging curve follows the typical pattern observed for lithium-sulfur batteries. The rapid increase in battery voltage at the end of the charging process in a Li—S battery is primarily due to the transition of polysulfides to elemental sulfur, which involves a significant change in electrochemical potential and reduction in ionic conductivity, leading to higher resistance and thus a steep rise in voltage. After self-charging, the PSC-LSB energy module was discharged to 1.7 V at 0.1C (based on the 1675 mAh/g), as depicted in Fig. 4(d). The two discharge plateau voltages in the module represent the reduction of S8 to long-chain polysulfides (Li_2S_x, $4 \leq x \leq 8$) and, finally, to the short-chain polysulfides (Li_2S_x, $1 \leq x \leq 2$). The first discharge capacity (74 mAh) is almost 100 % of the theoretical capacity of the designed sulfur electrode (based on 1001 mAh/g as shown in Fig. 3(f)). Fig. 4(e) shows the cycle stability with the discharge capacity over 200 cycles at a rate of 0.1C-rate. The discharge capacity after 200 cycles is approximately 66.4 mAh, indicating excellent cycle life performance with 87 % retention. The PSE, a critical property of an integrated energy module, can be calculated using the following equation:

$$PSE(\%) = \frac{P_{discharge}}{P_{insolation}} \times 100\%$$

where $P_{insolation}$ is the energy (Wh/m^2) of the light source, and $P_{discharge}$ is the discharge energy of the LSB part. With a light source energy of 30 Wh/m^2 provided to the PSC, and the LSB delivering 4.4 Wh/m^2 in a discharge state of 0.1C, the unprecedented PSE obtained was 14.6 %. This result is superior to those reported for integrated energy devices. [1–5,7–13] In particular, when compared to previous works on energy-integrated modules using solar cells and LSB, our PV cells exhibited exceptional output performance and strong operational stability under AM 1.5 illumination, contributing to achieving a record PSE among any work reported to date as shown Table S1 and S2. The high discharge capacity and stable lifespan of the PSC-LSB energy module may be attributed to efficient charging by a common substrate without energy loss and improved electrical conductivity through the porous carbon composite sulfur electrode.

4. Conclusion

In this study, we introduced a novel design featuring an integrated perovskite solar cell (PSC) as an energy conversion component and a lithium-sulfur battery (LSB) as an energy storage component, with both components connected by metal patterning on a common substrate. The materials for energy conversion and storage were optimized for high efficiency, and the series-connected PSCs provided a stable charging voltage of 3.0 V with an efficiency of 16.2 %. The LSB, utilizing sulfur-composited porous carbon fibers (S-CC66), achieved a discharging capacity of 1001.1 mAh/g at a current density of 0.1C. The PSE of the integrated PSC-LSB energy module reached an impressive 14.6 %, surpassing any reported integrated energy devices. The PSC-LSB energy module exhibited an 87 % retention in discharge capacity, maintaining stable performance after 200 cycles. The exceptional properties of the PSC-LSB energy integrated module can be attributed to the carefully selected materials for the PSC and LSB, as well as efficient connection through metal patterning on the common substrate. The outstanding performance of the on-chip PSC-LSB energy module suggests that the metal pattern-based self-charging energy device developed in this work may pave the way for high-energy and effective semi-permanent energy systems with a new charge mode. The energy-integrated self-charging modules can be applied to valuable applications such as wearable devices (for continuous charging of wearable healthcare devices and fitness trackers), drones and unmanned aerial vehicles (for recharging during missions, extending flight time), remote sensing and environmental monitoring (for continuous operation of such equipment), and portable medical devices (to extend battery life). Additionally, perovskite-based devices can feasibly be up-scaled using large-area deposition techniques to realize large-area modules for enhanced power generation. Therefore, this innovative approach holds promise for advancing the field of energy storage and conversion technologies.

Supplementary data to this article can be found online at https://doi.org/10.1016/j.est.2024.114149.

CRediT authorship contribution statement

Jae-Kwang Kim: Writing – original draft, Methodology, Writing – review & editing, Conceptualization, Formal analysis, Data curation. **Jun Ryu:** Writing – review & editing, Formal analysis, Conceptualization, Methodology, Writing – original draft. **Chaeeun Kang:** Methodology, Investigation. **Jooeun Park:** Software, Resources. **Jeha Kim:** Validation. **Jung Sang Cho:** Visualization. **Dong-Won Kang:** Writing – review & editing, Supervision, Project administration, Funding acquisition, Conceptualization. **Sang Mun Jeong:** Supervision, Funding acquisition, Conceptualization, Writing – review & editing.

Declaration of competing interest

The authors declare that they have no known competing financial interests or personal relationships that could have appeared to influence the work reported in this paper.

Acknowledgements

This research was supported by the National Research Foundation of Korea (NRF) grant funded by the Korea government (MSIT) (NRF - 2021R1A4A2001687).

Data availability

Data will be made available on request.

References

[1] J. Du, Q. Liao, M. Hong, B. Liu, X. Zhang, H. Yu, J. Xiao, L. Gao, F. Gao, Z. Kang, Piezotronic effect on interfacial charge modulation in mixed-dimensional van der Waals heterostructure for ultrasensitive flexible photodetectors, Nano Energy 58 (2019) 85–93, https://doi.org/10.1016/j.nanoen.2019.01.024.

[2] S. Park, S.W. Heo, W. Lee, D. Inoue, Z. Jiang, K. Yu, H. Jinno, D. Hashizume, M. Sekino, T. Yokota, Self-powered ultra-flexible electronics via nano-grating-patterned organic photovoltaics, Nature 561 (2018) 516–521, https://doi.org/10.1038/s41586-018-0536-x.

[3] C. Li, S. Cong, Z. Tian, Y. Song, L. Yu, C. Lu, Y. Shao, J. Li, G. Zou, M.H. Rümmeli, Flexible perovskite solar cell-driven photo-rechargeable lithium-ion capacitor for self-powered wearable strain sensors, Nano Energy 60 (2019) 247–256, https://doi.org/10.1016/j.nanoen.2019.03.061.

[4] H. Kim, T.Y. Jung, Independent solar photovoltaic with energy storage systems (ESS) for rural electrification in Myanmar, Renew. Sustain. Energy Rev. 82 (2018) 1187–1194, https://doi.org/10.1016/j.rser.2017.09.037.

[5] X. Pu, Z.L. Wang, Self-charging power system for distributed energy: beyond the energy storage unit, Chem. Sci. 12 (2021) 34–49, https://doi.org/10.1039/D0SC05145D.

[6] A. Azarpour, S. Suhaimi, G. Zahedi, A. Bahadori, A review on the drawbacks of renewable energy as a promising energy source of the future, Arab. J. Sci. Eng. 38 (2013) 317–328, https://doi.org/10.1007/s13369-012-0436-6.

[7] J. Zhao, L. Li, Y. Zhang, C. Li, Q. Zhang, J. Peng, X. Zhao, Q. Li, X. Wang, J. Xie, Novel coaxial fiber-shaped sensing system integrated with an asymmetric supercapacitor and a humidity sensor, Energy Stor. Mater. 15 (2018) 315–323, https://doi.org/10.1016/j.ensm.2018.06.007.

[8] O.H. Kwon, J. Ryu, J.H. Lee, H.W. Kim, J.S. Cho, S.M. Jeong, D.-W. Kang, J.-K. Kim, Stretchable self-charging energy integrated device of high storage efficiency, J. Power Sources 525 (2022) 231079, https://doi.org/10.1016/j.jpowsour.2022.231079.

[9] T.-T. Li, Y.-B. Yang, B.-S. Zhao, Y. Wu, X.-W. Wu, P. Chen, X.-P. Gao, Photo-rechargeable all-solid-state lithium−sulfur batteries based on perovskite indoor photovoltaic modules, J. Chem. Eng. 455 (2023) 140684, https://doi.org/10.1016/j.cej.2022.140684.

[10] D. Lau, N. Song, C. Hall, Y. Jiang, S. Lim, I. Perez-Wurfl, Z. Ouyang, A. Lennon, Hybrid solar energy harvesting and storage devices: the promises and challenges, mater. Today, Energy 13 (2019) 22–44, https://doi.org/10.1016/j.mtener.2019.04.003.

[11] P. Chen, G.R. Li, T.T. Li, X.P. Gao, Solar-driven rechargeable lithium–sulfur battery, Adv. Sci. 6 (2019) 1900620, https://doi.org/10.1002/advs.201900620.

[12] Z. Tian, X. Tong, G. Sheng, Y. Shao, L. Yu, V. Tung, J. Sun, R.B. Kaner, Z. Liu, Printable magnesium ion quasi-solid-state asymmetric supercapacitors for flexible solar-charging integrated units, Nat. Commun. 10 (2019) 4913, https://doi.org/10.1038/s41467-019-12900-4.

[13] D.S. Gardner, C.W. Holzwarth III, Y. Liu, S.B. Clendenning, W. Jin, B.-K. Moon, C. Pint, Z. Chen, E.C. Hannah, C. Chen, Integrated on-chip energy storage using passivated nanoporous-silicon electrochemical capacitors, Nano Energy 25 (2016) 68–79, https://doi.org/10.1016/j.nanoen.2016.04.016.

[14] S.D. Stranks, G.E. Eperon, G. Grancini, C. Menelaou, M.J. Alcocer, T. Leijtens, L. M. Herz, A. Petrozza, H.J. Snaith, Electron-hole diffusion lengths exceeding 1 micrometer in an organometal trihalide perovskite absorber, Science 342 (2013) 341–344, https://doi.org/10.1126/science.1243982.

[15] H. Oga, A. Saeki, Y. Ogomi, S. Hayase, S. Seki, Improved understanding of the electronic and energetic landscapes of perovskite solar cells: high local charge carrier mobility, reduced recombination, and extremely shallow traps, J. Am. Chem. Soc. 136 (2014) 13818–13825, https://doi.org/10.1021/ja506936f.

[16] T.C. Sum, N. Mathews, Advancements in perovskite solar cells: photophysics behind the photovoltaics, Energ. Environ. Sci. 7 (2014) 2518–2534, https://doi.org/10.1039/C4EE00673A.

[17] S. Gholipour, M. Saliba, Bandgap Tuning and Compositional Exchange for Lead Halide Perovskite Materials, Characterization Techniques for Perovskite Solar Cell Materials, Elsevier, in, 2020, pp. 1–22.

[18] M.A. Green, A. Ho-Baillie, H.J. Snaith, The emergence of perovskite solar cells, Nat. Photonics 8 (2014) 506–514, https://doi.org/10.1038/nphoton.2014.134.

[19] H.S. Jung, N.G. Park, Perovskite solar cells: from materials to devices, Small 11 (2015) 10–25, https://doi.org/10.1002/smll.201402767.

[20] NREL, Best Research-Cell Efficiency Chart. https://www.nrel.gov/pv/cell-efficiency.html (accessed 20 December 2023).

[21] G. Xing, N. Mathews, S. Sun, S.S. Lim, Y.M. Lam, M. Grätzel, S. Mhaisalkar, T. C. Sum, Long-range balanced electron-and hole-transport lengths in organic-inorganic $CH_3NH_3PbI_3$, Science 342 (2013) 344–347, https://doi.org/10.1126/science.1243167.

[22] Z. Guo, A.K. Jena, G.M. Kim, T. Miyasaka, The high open-circuit voltage of perovskite solar cells: a review, Energ. Environ. Sci. 15 (2022) 3171–3222, https://doi.org/10.1039/D2EE00663D.

[23] P. Holzhey, M. Prettl, S. Collavini, N.L. Chang, M. Saliba, Toward commercialization with lightweight, flexible perovskite solar cells for residential photovoltaics, Joule 7 (2023) 257–271, https://doi.org/10.1016/j.joule.2022.12.012.

[24] H.J. Snaith, Perovskites: the emergence of a new era for low-cost, high-efficiency solar cells, J. Phys. Chem. Lett. 4 (2013) 3623–3630, https://doi.org/10.1021/jz4020162.

[25] H. Yu, J.S. Han, G.C. Hwang, J.S. Cho, D.-W. Kang, J.-K. Kim, Optimization of high potential cathode materials and lithium conducting hybrid solid electrolyte for high-voltage all-solid-state batteries, Electrochim. Acta 365 (2021) 137349, https://doi.org/10.1016/j.electacta.2020.137349.

[26] S.Y. Kim, S.J. Cho, S.E. Byeon, X. He, H.J. Yoon, Self-assembled monolayers as interface engineering nanomaterials in perovskite solar cells, Adv. Energy Mater. 10 (2020) 2002606, https://doi.org/10.1002/aenm.202002606.

[27] S. Asgary, H.M. Moghaddam, A. Bahari, R. Mohammadpour, Role of BCP layer on nonlinear properties of perovskite solar cell, Sol. Energy 213 (2021) 383–391, https://doi.org/10.1016/j.solener.2020.11.040.

[28] J. Li, H.A. Dewi, H. Wang, J.H. Lew, N. Mathews, S. Mhaisalkar, A. Bruno, Design of Perovskite Thermally co-Evaporated Highly Efficient Mini-Modules with high geometrical fill factors, Sol. RRL 4 (2020) 2000473, https://doi.org/10.1002/solr.202000473.

[29] S. Li, Z. Fan, Encapsulation methods of sulfur particles for lithium-sulfur batteries: a review, Energy Stor. Mater. 34 (2021) 107–127, https://doi.org/10.1016/j.ensm.2020.09.005.

[30] Y. Li, S. Guo, Material design and structure optimization for rechargeable lithium-sulfur batteries, Matter 4 (2021) 1142–1188, https://doi.org/10.1016/j.matt.2021.01.012.

[31] Y. Liu, D.J. Lee, K.-K. Cho, Y. Zou, H.-J. Ahn, J.-H. Ahn, Promoting long cycle life with honeycomb-like tri-modal porous carbon for stable lithium-sulfur polymer batteries, J. Alloys Compd. 932 (2023) 167704, https://doi.org/10.1016/j.jallcom.2022.167704.

[32] J. Song, T. Xu, M.L. Gordin, P. Zhu, D. Lv, Y.B. Jiang, Y. Chen, Y. Duan, D. Wang, Nitrogen-doped mesoporous carbon promoted chemical adsorption of sulfur and fabrication of high-areal-capacity sulfur cathode with exceptional cycling stability for lithium-sulfur batteries, Adv. Funct. Mater. 24 (2014) 1243–1250, https://doi.org/10.1002/adfm.201302631.

[33] H. Byeon, B. Gu, H.-J. Kim, J.H. Lee, I. Seo, J. Kim, J.W. Yang, J.-K. Kim, Redox chemistry of nitrogen-doped CNT-encapsulated nitroxide radical polymers for high energy density and rate-capability organic batteries, Chem. Engineering J. 413 (2021) 127402, https://doi.org/10.1016/j.cej.2020.127402.